

Sizing BESS and On-site Renewable for Battery-electric Freight Rail Charging Station

Vinson Guov
School of EECS
Oregon State University
Corvallis, Oregon, U.S.A.
guovv@oregonstate.edu

Derek Jackson
School of EECS
Oregon State University
Corvallis, Oregon, U.S.A.
jacksder@oregonstate.edu

Yue Cao
School of EECS
Oregon State University
Corvallis, Oregon, U.S.A.
Yue.Cao@oregonstate.edu

Abstract—Although freight rail is one of the most energy-efficient modes of freight transport, there is increasing pressure to cut greenhouse gas (GHG) emissions in light of climate change. Since catenary (i.e., overhead wire) electric locomotives are not appealing in the U.S. due to the private ownership nature of railways, this paper presents a tool to predict the sizing and cost of deploying battery-electric freight rail fast charging stations, which will integrate with a network train simulator to examine various energy pathways to decarbonizing U.S. rail. Fast-charging stations at the power level >1 MW require a demand buffer between the grid and pulsed charging loads, especially in remote rural areas. To mitigate grid demand while ensuring efficient emission-free power sourcing, on-site BESS and renewable energy sources are used. Steady-state models are developed for each station subsystem, including multiple options for energy storage, renewable sources, and power electronics. Charging station behavior is simulated using realistic input data. The tool uses the simulator to produce optimally-sized designs through multi-objective optimization to facilitate trade-off comparisons between the BESS and on-site renewables.

Index Terms—Freight rail, electric vehicles, trains, DC fast charging station, DC microgrid, energy storage, solar PV, wind, power electronics, sizing, load leveling, optimization

I. INTRODUCTION

In the U.S. in 2019, 24,597 Class I freight locomotives consumed 3.4 billion gallons of diesel fuel and emitted 37.6 million metric tons of CO₂ [1], [2]. Although it is considerably more fuel-efficient to transport freight by rail than by freight truck, there has been increasing demand to ship freight via rail intermodal over the past several years [3]. Since the current target of the U.S. government is to achieve net zero emissions by 2050, greenhouse gas (GHG) emissions must also be curbed in the freight rail sector [4]. The competing freight truck sector is approaching this emissions reduction by electrifying its fleet via battery-electric or hydrogen fuel cell, and installing onboard carbon capture for existing freight truck diesel engines. Since the lifetime of locomotives is long (>20 years), there is significant reluctance in the U.S. rail industry to replace their existing diesel-electric locomotive fleet. Catenary is another option in rail electrification, but is unappealing due to its high installation and maintenance costs [5]. In the near future, the freight rail industry expects to retrofit its existing locomotives with compatible biodiesel and renewable diesels to drive emissions down. However, far into the future,

full decarbonization is expected. This paper addresses the sizing of fast charging stations (FCS) where battery-electric locomotives and battery tenders will be recharged along freight rail corridors and at railyards.

The design challenges surrounding freight rail FCSs are similar to those encountered by road passenger electric vehicle FCSs. However, the peak power delivered by the station is much greater (e.g., 1 MW), the demand patterns differ, and the charging locations may be more rural. The highly pulsed load from freight rail FCSs will be detrimental to grid power quality, and rural grids will be especially sensitive to this additional intermittent loading. This can be mitigated by using co-located renewable energy and energy storage [6].

For true locomotive decarbonization, the sourced power must come from zero-emission sources. Local renewables can ensure power is coming from a renewable source while also reducing the burden on the local grid, which also reduces power transmission losses. A battery energy storage system (BESS) can improve the utilization of local renewable energy generation while also significantly reducing electricity demand cost and electrical service size from the AC grid.

With multiple energy systems operating simultaneously, management of power flow between the systems requires a microgrid. A DC microgrid is preferred for its fewer power conversion stages (and higher efficiency) compared to AC, but currently lacks maturity due to lack of standardization [7]. Since this paper focuses on the future electrification of rail, the maturity of DC microgrid technology is expected.

To plan for a future with zero-emission locomotives, this paper presents a tool used to predict the sizing/cost of locomotive charging infrastructure. This will integrate with a network train simulator that spans temporally and spatially to provide an economic analysis on different pathways for decarbonizing rail in the U.S. [8]. The tool sizes on-site renewable and BESS capacities for a battery-electric freight rail FCS, using realistic power loss models and resource data to represent the temporally variable renewable power and pulsed charging load, similar to the solar insolation and load profile data used in [9]. This presents itself as a multi-objective optimization problem, since the sizing of the battery system affects the sizing of the renewable system.

The objectives are to minimize the renewable and BESS

system capacities. A multi-objective optimization approach is applied to find all optimally sized FCS designs. Similar to [10], the optimization is constrained by assuming the primary load is always met. This is used to identify feasible designs where the FCS is able to meet the load at any given time without violating other optimization constraints. The optimization results are presented as a Pareto front, showcasing the trade-offs between the two sizing objectives, where the economic benefits of each optimal design can be considered.

Since it is uncertain which renewable and BESS technologies in the future will be most cost-effective for a particular FCS, this tool models two renewable sources and two BESS technologies: 1) solar PV and wind, 2) lithium-ion and redox flow, respectively. Renewable resources vary geographically, so it is pertinent to present multiple renewable resources options. The battery models can be easily adapted for different chemistries, such as lead-acid, vanadium, or iron.

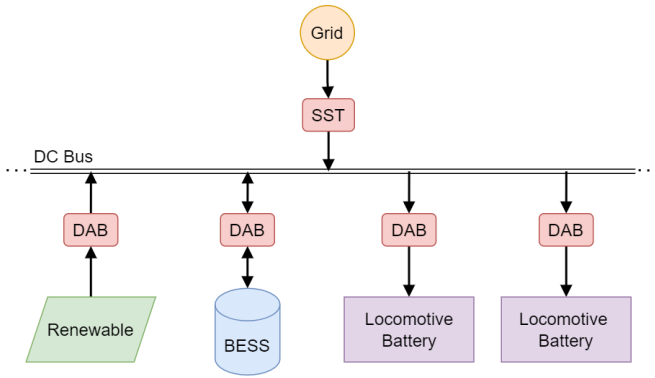


Fig. 1. Fast charging station architecture

II. FREIGHT RAIL CHARGING STATION MODELING

The freight rail FCS is represented by Fig. 1, a DC microgrid consisting of renewable energy sources, BESS, locomotive battery chargers, and an AC grid connection. Each subsystem connects to a common DC bus through power electronic converters. Power from the AC grid is rectified through a solid-state transformer (SST) to the DC bus, while dual-active bridge (DAB) converters handle the DC/DC power conversion between the microgrid systems.

A. Battery Energy Storage System

The two energy storage mediums considered in this paper are Lithium-ion batteries (LIB) and Vanadium redox flow batteries (VRFB). Lithium-ion batteries are a popular choice because of their high specific energy/power and declining cost [11]. Redox flow batteries are attractive for large stationary energy storage applications because the capacity is easily scalable and exhibits long cycle life without deep cycling penalty [12].

1) *Lithium-Ion Battery*: The LIB model is based on the parametric battery model from [13]. The battery cell terminal voltage V_{Li} is determined using (1), where V_{oc} is the open-circuit voltage, i_{Li} is the current, and R_{ser} is the series

resistance of the cell. Since R_{ser} and V_{oc} are a function of state of charge (SOC), the curve-fitting method in [13] shown in (2) is used, where the coefficients a_k are determined from battery test measurements. The series resistance and capacitance at various time frames (seconds, minutes, hours) in (1) are neglected since the simulation is steady-state. To model the entire array of battery cells within the BESS, V_{Li} and i_{Li} are simply scaled by the number of cells in series ($N_{LIB,ser}$) and in parallel ($N_{LIB,par}$), respectively, to obtain the BESS terminal output voltage V_{LIB} and current i_{LIB} . This leads to the calculation of total power drawn from the BESS with (5).

$$V_{Li} = V_{oc} - i_{Li} \cdot (R_{ser} + R_s \parallel \frac{1}{sC_s} + R_m \parallel \frac{1}{sC_m} + R_h \parallel \frac{1}{sC_h}) \quad (1)$$

$$V_{oc}, R_{ser} = \exp \left[\sum_{k=0}^6 a_k \ln^k(\text{SOC}) \right] \quad (2)$$

$$V_{LIB} = N_{LIB,ser} V_{Li} \quad (3)$$

$$i_{LIB} = N_{LIB,par} i_{Li} \quad (4)$$

$$P_{LIB} = V_{LIB} i_{LIB} \quad (5)$$

To determine the energy stored and SOC of the BESS at the end of each simulation time interval, (7) and (8) are used, where t_1 and t_2 are the previous and current time step. $E_{LIB,max}$ is calculated in (6), using the average cell voltage $\overline{V_{Li}}$ and rated Amp-hours Ah_{Li} .

$$E_{LIB,max} = N_{LIB,ser} N_{LIB,par} \overline{V_{Li}} Ah_{Li} \quad (6)$$

$$E_{LIB} = E_{LIB,max} \text{SOC}(t_1) - \int_{t_1}^{t_2} P_{LIB} dt \quad (7)$$

$$\text{SOC}(t_2) = E_{LIB} / E_{LIB,max} \quad (8)$$

2) *Vanadium Redox Flow Battery*: The VRFB consists of a catholyte tank, anolyte tank, and several electrochemical cell stack. The electrochemical cell terminal voltage V_{RF} is found using (9) from [12], where E_0 is a reference cell voltage of 1.37 V at 0.5 SOC, R is the universal gas constant, and T is the battery's electrolyte absolute temperature.

$$V_{RF} = E_0 + \frac{2RT}{F} \ln\left(\frac{\text{SOC}}{1-\text{SOC}}\right) \quad (9)$$

To determine the flowrate required to continuously supply sufficient ions to the electrochemical cells, (10) from [14] is used, where i_{stack} is the current out of the electrochemical cell stack, n_e is the number of electrons transferred per mole of Vanadium species consumed during electrolysis, c is the Vanadium concentration in the electrolyte, and F is Faraday's Constant.

$$Q = \frac{i_{stack}}{n_e c F \text{SOC}} \quad (10)$$

(11) uses flow rate Q from (10), hydraulic resistance R_{hydr} (of the entire hydraulic system, assuming laminar flow), and pump efficiency η_{pump} to calculate the electrical power required to operate the two pumps for the catholyte/anolyte tanks.

$$P_{pump} = \frac{2 Q^2 R_{hydr}}{\eta_{pump}} \quad (11)$$

The RFB Amp-hour capacity, in terms of Liters of electrolyte L in each tank, is calculated using (12) before the energy stored or SOC can be determined in (13).

$$\text{Ah}_{RFB} = \frac{F}{3600} c L \quad (12)$$

$$E_{RFB,max} = \text{Ah}_{RFB} N_{RFB,ser} E_0 \quad (13)$$

To calculate the energy drawn from the RFB after each simulation time interval, the power losses calculated in (14) are summed with the RFB power output to find the total power P_{RFB} in (15). J is the current density at the cell electrodes, and R_{cell} is the specific resistance of one cell. This power is then integrated in (16) to find E_{RFB} , where t_1 and t_2 are the previous and current time step. Similar to the LIB battery model, (17) calculates $\text{SOC}(t_2)$.

$$P_{RFB,loss} = N_{ser} J^2 R_{cell} + P_{pump} \quad (14)$$

$$P_{RFB} = N_{RFB,ser} V_{RF} \dot{i}_{stack} + P_{RFB,loss} \quad (15)$$

$$E_{RFB} = E_{RFB,max} \text{SOC}(t_1) - \int_{t_1}^{t_2} P_{RFB} dt \quad (16)$$

$$\text{SOC}(t_2) = E_{RFB}/E_{RFB,max} \quad (17)$$

B. Renewables

1) *Solar PV Farm*: The model developed assumes solar irradiance and power output of the plant are directly proportional. The power output of the solar farm is calculated with (18) from [19]. η_{pv} is the efficiency of the power electronics (assumed to be constant), N_p is the number of parallel cells/modules, N_s is the number of cells/modules in series, V_o is the open-circuit cell/module voltage, I_s is the short-circuit cell/module current, FF is the fill factor, E is the solar irradiance, and E_{ref} is the reference irradiance where V_{oc} and I_{sc} were tested at.

$$P_{PV}(E) = \eta_{pv} N_p N_s V_o I_s \text{FF} \frac{E}{E_{ref}} \quad (18)$$

2) *Wind Turbine Farm*: The wind turbine farm model assumes an array of horizontal-axis wind turbines (HAWT), where the power output of the wind farm is proportional to the cube of wind speed between the wind turbine cut-in wind speed v_{cut_in} and rated wind speed v_{rated} . Eq. (19) from [19] calculates the available wind power, where C_p is the coefficient of power, ρ is the air density, v is the wind speed at the hub height, and A is the swept area of the rotor. Eq. (19)

is used in (21) as part of the piecewise function to determine wind farm power output. Between v_{rated} and v_{cut_out} , P_W is constant as described by (20). η_{tb} is a coefficient (assumed to be constant) representing losses due to mechanical/electrical energy conversion in the turbines. N_{tb} is the number of wind turbines in the farm.

$$P_{wind} = \frac{1}{2} C_p \rho v^3 A \quad (19)$$

$$P_{rated} = \frac{1}{2} C_p \rho v_{rated}^3 A \quad (20)$$

$$P_W(v) = \begin{cases} 0 & v \leq v_{cut_in} \\ \eta_{tb} N_{tb} P_{wind} & v_{cut_in} \leq v \leq v_{rated} \\ \eta_{tb} N_{tb} P_{rated} & v_{rated} \leq v \leq v_{cut_out} \\ 0 & v \geq v_{cut_out} \end{cases} \quad (21)$$

C. Power Converter Modeling

Power losses can become significant given the magnitude of energy managed by the charging station. Effective sizing of the energy storage system and renewable energy assets should then consider accurate power converter loss models. This subsection outlines the steady-state power loss modeling of the DAB DC/DC converters and SST AC/DC rectifier used in the power conversion stages. Rather than considering constant efficiency, utilizing these power loss models more accurately captures the system efficiency under varying loads and generation.

1) *Dual-Active Bridge Converter*: As the power converters are not the focus of this paper, detailed discussion of their functionality is not included, but readers are referred to [15] and [16] for more information on the DAB. DAB power losses at steady-state are calculated using the approach in [15]. For a properly designed and controlled DAB, the inherent zero-voltage switching (ZVS) ability results in nearly zero switching losses and is thus omitted from the model [16]. The converter's total conduction loss is given by (22), where R_L is the transformer winding resistance, n_t is the secondary-primary winding turns ratio, and $R_{p,on}$ $R_{s,on}$ are the primary and secondary-side semiconductor drain-source on resistances, respectively. The transformer RMS current is calculated with (23) using the two peak transformer currents (24) and (25) [15]. A secondary-side reference is assumed for $I_{L,rms}$. In (23)-(25), the primary-secondary phase shift duty ratio is denoted as d , switching frequency as f_{sw} , and transformer leakage inductance is L_t .

$$P_{loss} = I_{L,rms}^2 \left[R_L + (4n_t^2 R_{p,on} + 4R_{s,on})/\sqrt{2} \right] \quad (22)$$

$$I_{L,rms} = \frac{1}{\sqrt{3}} \sqrt{dI_1^2 + (1-d)(I_1^2 + I_1I_2 + I_2^2)} \quad (23)$$

$$I_1 = \frac{1}{f_{sw} L_t} \left(V_{in} + \frac{V_o}{n_t} (2d - 1) \right) \quad (24)$$

$$I_2 = \frac{1}{f_{sw} L_t} \left(\frac{V_o}{n_t} + V_{in}(2d-1) \right) \quad (25)$$

Converter design details are simplified by connecting modular, lower rated DAB converters in parallel. To achieve the desired DAB power rating, the number of DAB converters in parallel N_{dcdc} is adjusted.

2) *Solid-State Transformer*: A thorough overview of SST configuration and operation can be found in [17]. The SST consists of a rectification stage and a voltage conversion/galvanic isolation stage and is often implemented using an H-bridge AC/DC converter and a DAB. Grid-connected SSTs in the literature are constructed by cascading multiple, modular H-bridge/DAB stages together to meet the necessary voltage and power ratings. Similar to the DAB converter, H-bridge conduction losses are given with (26), where $I_{sw,rms}$ is the RMS current experienced by each switch, and $R_{on,sw}$ is the drain-source on resistances. The RMS current is found using the input DC current of the DAB stage $I_{sw,rms} = \pi I_{dc}/2$, derived from the steady-state conditions. ZVS cannot be achieved in the H-bridge stage of an SST without additional circuit complexity and thus a switching loss model is needed. The averaged switching losses are calculated using (27) [18]. Under steady-state operating conditions, the DC link voltage between the H-bridge and DAB modules, V_{dc} in (27), can be assumed constant. The turn-on and turn-off commutation time t_{com} , and commutation parameter a_{com} are both obtained from the semiconductor's datasheet.

$$P_{con} = 4I_{sw,rms}^2 R_{on,sw} \quad (26)$$

$$P_{sw} = \frac{2V_{dc}I_{dc}t_{com}f_{sw}}{a_{com}} \quad (27)$$

To avoid exceeding semiconductor max-voltage and dv/dt ratings when connected to high-voltage distribution networks, modular SST units are often cascaded together [17]. For $N_{SST,s}$ SST units serially cascaded together and the grid line-neutral phase voltage V_{l-n} , each unit experiences an input voltage differential of $V_{l-n}/N_{SST,s}$. The SST power rating can be further increased by adjusting the number of SST units in parallel $N_{SST,p}$, and should be a multiple of 3 for a 3-phase input.

D. Energy Management System

The energy management system (EMS) in this FCS uses the load leveling approach to enforce a grid input power limit, using the BESS as a power buffer to reduce peak grid input power, significantly reducing demand charges and the size of the electrical service. If the locomotive charging load exceeds the grid power limit (determined from the average load power), the deficit is supplied by the on-site renewable and BESS, shown by the red area in Fig. 2. When the charging load is lower than the grid power limit, the surplus grid power charges the BESS, shown by the blue area in Fig. 2. This FCS cannot transfer power generated by the on-site renewable to the grid, so the on-site renewable is only used to charge the BESS or

to satisfy the load. The EMS also enforces SOC limits for the BESS to prevent under or overcharging.

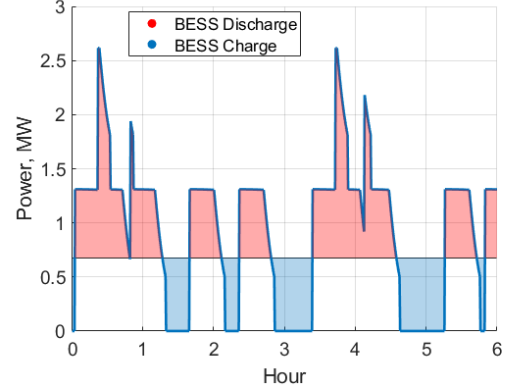


Fig. 2. Fast charging station load profile

III. INFRASTRUCTURE SIMULATION AND SIZING

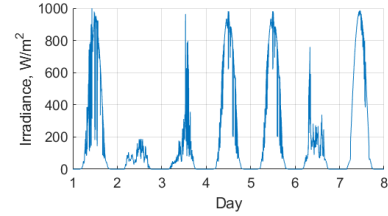


Fig. 3. Solar irradiance time series

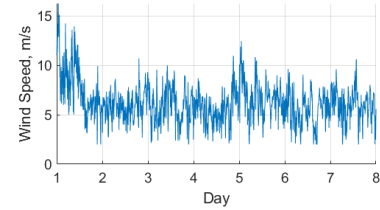


Fig. 4. Wind speed time series

A. Simulation Setup

Two week-long MATLAB simulations were performed to demonstrate the capabilities of the tool for sizing. To simulate all of the subsystems mentioned in Section II, one simulation has a RFB BESS and a solar PV farm, and the other has a LIB BESS and a wind turbine farm. The simulation time step is set to 1 minute to reduce simulation runtime for longer periods, such as months to years. Recalling the overview of the FCS shown in Fig. 1, the DC bus is 1500 V and the BESS nominal voltage is ~ 800 V. The FCS is connected to a 12.47 kV three-phase AC grid, rectified by the SST to the DC bus. This FCS has two DAB converters to enable simultaneous and independent charging of two locomotive packs. The locomotive battery packs' maximum voltage is ~ 1500 V.

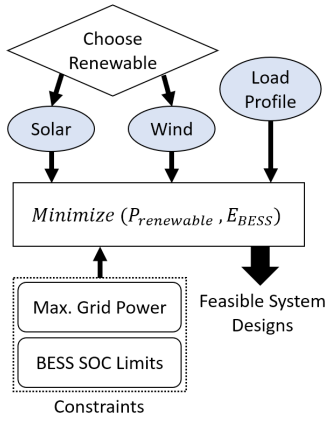


Fig. 5. Sizing process

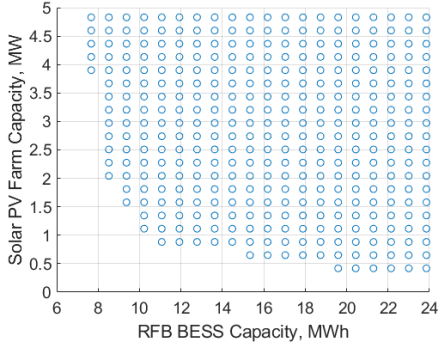


Fig. 6. RFB/PV feasible system designs

To accurately represent the temporal variability of the on-site renewables, high resolution solar irradiance from [20] and wind speed time series data from [21] is received by the simulation as an input to their respective renewable system models, shown in Fig. 3 and 4. The charging load time series, which represents the power demanded by the output of the two locomotive battery chargers, is shown in Fig. 2 for one of seven days. The peak power charging events peak at ~ 1.25 MW and last ~ 1 hour.

B. Sizing and Optimization

A multi-objective optimization approach is used to size the assets of the FCS, where the two objectives are to minimize the BESS energy capacity E_{BESS} and renewable plant capacity $P_{renewable}$, shown in Fig. 5. An exhaustive search is used to find the optimal designs. The tool simulates a range of possible design variable combinations while verifying the design feasibility. For the RFB BESS scenario, design variable E_{BESS} is adjusted by the tool in terms of liters of electrolyte, proportional to energy capacity. The solar PV plant design variable $P_{renewable}$ is adjusted by the number of parallel solar modules/panels. The various power electronic voltage/current ratings are governed by the chosen voltage ranges for the BESS and renewable systems.

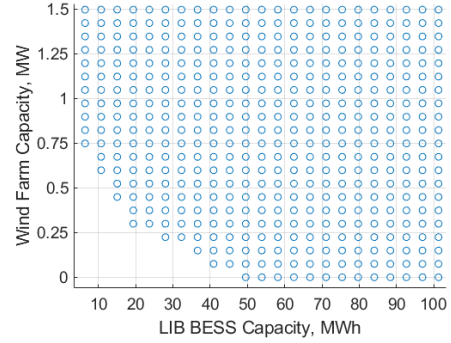


Fig. 7. LIB/Wind feasible system designs

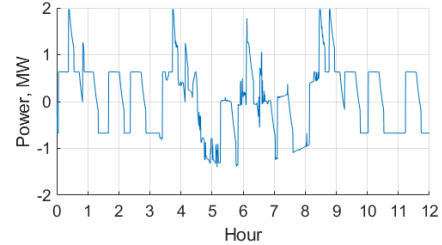


Fig. 8. RFB power output

A design is considered feasible if the following constraints are satisfied, where t_s is the set of all simulation time steps:

$$\min(\text{BESS}_{\text{SOC}}(t_s)) > \text{SOC}_{\text{limit,lower}} \quad (28)$$

$$\max(P_{\text{grid}}(t_s)) \leq P_{\text{grid,max}} \quad (29)$$

The BESS SOC upper limit $\text{SOC}_{\text{limit,upper}}$ is managed by the EMS described in Section II-D, but exceeding the lower limit $\text{SOC}_{\text{limit,lower}}$ will result in a failed design, since that implies the BESS is no longer providing sufficient energy to the FCS. The grid power limit is technically a constraint but is enforced by the EMS. Since the power converter ratings are determined based on the max power of each subsystem (BESS, renewable, grid connection, battery chargers), such constraints would be inactive.

C. Results Discussion

With the two simulations performed, the sizing results from both scenarios are presented in Fig. 6 and 7. The blue circles indicate the feasible designs the tool found during sizing. The tool successfully discovered the Pareto front (or Pareto-efficient solutions) of the sizing problem at the boundary between the blue circles and white space. When comparing the two design spaces, the LIB/Wind combination has a narrower Pareto front than the RFB/PV combination. This can be explained by the lower capacity factor of solar PV, which increases the uncertainty of energy generated at any given time. When combined with the network train simulator, feasible FCS designs will determine the most cost-effective BESS and on-site renewable combinations, which will be unique to each FCS site due to different constraints and costs.

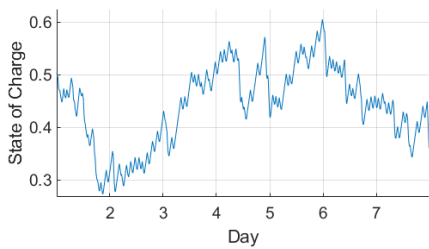


Fig. 9. LIB state of charge

Fig. 8 and 9 show the RFB power output and LIB SOC, respectively, during one of many simulations performed by the tool. The RFB power output is continuously switching directions due to the highly pulsed load profile, and is more negatively biased around solar noon during the first day of the week-long simulation because of the peak power delivered by the solar PV farm. Although not included in this paper, the LIB/Wind combination yielded a more predictable BESS power output since wind power is more consistent than solar power. Fig. 9 demonstrates the SOC variation throughout a simulation, which never exceeds the prescribed SOC limits.

IV. CONCLUSION

This paper describes an approach for simulating the behavior of a battery-electric freight rail fast charging station to find the multi-objective trade-offs between the on-site BESS and renewable energy source sizes, based on realistic resource data describing the pulsed nature of the charging loads and temporally variable renewable power. An approach to modeling the charging station subsystems has been presented, which includes the power electronics, BESS, and renewables. The integration of these subsystems to simulate two FCSs is demonstrated in this paper, with results indicating Pareto optimal designs that can be used by a higher-level network train simulator to drive economic modeling of charging infrastructure to discover feasible pathways to decarbonizing freight rail in the U.S. or other parts of the world where applicable. The FCS simulation in this paper was one week long, but could be extended to one year for a more accurate representation of seasonal variations in renewable power and locomotive refueling activity.

ACKNOWLEDGMENT

This work was supported in part by the U.S Department of Energy (DOE) Advanced Research Projects Agency - Energy (ARPA-E) Award under Grant DE-AR0001471, and in part by the U.S. National Science Foundation (NSF) Award ECCS-2146350.

REFERENCES

[1] *Rail Profile*. Accessed on December 13, 2021. [Online]. Available: <https://www.bts.gov/content/rail-profile>.
 [2] "Fast Facts on Transportation Greenhouse Gas Emissions," EPA. Accessed on December 13, 2021. [Online]. Available: <https://www.epa.gov/greenvehicles/fast-facts-transportation-greenhouse-gas-emissions>.

[3] "What Railroads Haul: Intermodal." Accessed on December 13, 2021. [Online]. Available: <https://www.aar.org/wp-content/uploads/2020/07/AAR-Intermodal-Fact-Sheet.pdf>.
 [4] "The Long-Term Strategy of the United States: Pathways to Net-Zero Greenhouse Gas Emissions by 2050." Accessed on May 15, 2022. [Online]. Available: <https://www.whitehouse.gov/wp-content/uploads/2021/10/US-Long-Term-Strategy.pdf>
 [5] "Oppose Rail Electrification & Support Sensible Climate Policy." Accessed on December 13, 2021. [Online]. Available: <https://www.railwayage.com/wp-content/uploads/2021/02/AAR-Electrification-Fact-Sheet.pdf>.
 [6] L. Wang, Z. Qin, T. Slangen, P. Bauer and T. van Wijk, "Grid Impact of Electric Vehicle Fast Charging Stations: Trends, Standards, Issues and Mitigation Measures - An Overview," *IEEE Open Journal of Power Electronics*, vol. 2, pp. 56-74, 2021.
 [7] H. Tu, H. Feng, S. Srdic and S. Lukic, "Extreme Fast Charging of Electric Vehicles: A Technology Overview," *IEEE Transactions on Transportation Electrification*, vol. 5, no. 4, pp. 861-878, Dec. 2019.
 [8] Advanced Research Projects Agency - Energy (ARPA-E), U.S. Department of Energy, "Multi-decadal Decarbonization Pathways for U.S. Freight Rail - DE-FOA-0001953", <https://arpa-e-foa.energy.gov/>, 2021, [Accessed: 12.20.2021].
 [9] M. B. Shadmand and R. S. Balog, "Multi-Objective Optimization and Design of Photovoltaic-Wind Hybrid System for Community Smart DC Microgrid," in *IEEE Transactions on Smart Grid*, vol. 5, no. 5, pp. 2635-2643, Sept. 2014.
 [10] T. A. Nguyen, M. L. Crow and A. C. Elmore, "Optimal Sizing of a Vanadium Redox Battery System for Microgrid Systems," in *IEEE Transactions on Sustainable Energy*, vol. 6, no. 3, pp. 729-737, July 2015.
 [11] B. Dunn, H. Kamath, and J.-M. Tarascon, "Electrical Energy Storage for the grid: A battery of choices," *Science*, vol. 334, no. 6058, pp. 928-935, 2011.
 [12] M. Guarnieri, P. Mattavelli, G. Petrone and G. Spagnuolo, "Vanadium Redox Flow Batteries: Potentials and Challenges of an Emerging Storage Technology," *IEEE Industrial Electronics Magazine*, vol. 10, no. 4, pp. 20-31, Dec. 2016.
 [13] Y. Cao, R. C. Kroeze and P. T. Krein, "Multi-timescale Parametric Electrical Battery Model for Use in Dynamic Electric Vehicle Simulations," *IEEE Transactions on Transportation Electrification*, vol. 2, no. 4, pp. 432-442, Dec. 2016.
 [14] A. Bhattacharjee and H. Saha, "Design and experimental validation of a generalised electrical equivalent model of vanadium redox flow battery for interfacing with Renewable Energy Sources," *Journal of Energy Storage*, vol. 13, pp. 220-232, 2017.
 [15] K. George, "Design and Control of a Bidirectional Dual Active Bridge DC-DC Converter to Interface Solar, Battery Storage, and Grid-Tied Inverters," Electrical Engineering Undergraduate Honors Thesis, University of Arkansas, 2015.
 [16] H. Ramakrishnan, "Bi-Directional, Dual Active Bridge Reference Design for Level 3 Electric Vehicle Charging Stations," Texas Instruments Incorporated, Design Guide: TIDA-010054, 2019.
 [17] Lahooti Eshkevari, A., Mosallanejad, A. and Sepasian, M., "In-depth study of the application of solid-state transformer in design of high-power electric vehicle charging stations," *IET Electr. Syst. Transp.*, vol. 10, pp.310-319, 2020.
 [18] P. T. Krein, *Elements of Power Electronics*, 2nd ed. New York: Oxford University Press, 2015, pp 437-439.
 [19] J. Andrews, *Energy science: Principles, technologies, and impacts*, 3rd ed. Oxford University Press, 2017.
 [20] Y. Cao, J. A. Magerko, R. Serna, S. Qin, R. C. N. Pilawa-Podgurski and P. T. Krein, "One Year Submillisecond Fast Solar Database: Collection, Investigation, and Application," *2019 IEEE Energy Conversion Congress and Exposition (ECCE)*, 2019, pp. 2047-2053.
 [21] Diamond, H. J., T. R. Karl, M. A. Palecki, C. B. Baker, J. E. Bell, R. D. Leeper, D. R. Easterling, J. H. Lawrimore, T. P. Meyers, M. R. Helfert, G. Goodge, and P. W. Thorne, 2013 : U.S. Climate Reference Network after one decade of operations: status and assessment. *Bull. Amer. Meteor. Soc.* , 94 , 489-498.